PHYSICAL REVIEW C VOLUME 45, NUMBER 3 MARCH 1992

Fast-neutron interaction with elemental zirconium, and the dispersive optical model

S. Chiba,* P. T. Guenther, A. B. Smith, M. Sugimoto,* and R. D. Lawson
Argonne National Laboratory, 9700 South Cass Avenue, Argonne, Illinois 60439

(Received 25 July 1991)

Differential neutron elastic- and inelastic-scattering cross sections of elemental zirconium were measured from ≈ 1.5 to 10 MeV. Below 3 MeV the measurements were made at incident-neutron energy intervals of ≈ 100 keV, from 3 to 4 MeV in steps of ≈ 200 keV, and in ≈ 500 keV increments at higher energies. The angular range of the measurements is $\approx 18°$ to 160°, with up to more than 100 differential values per distribution. This comprehensive database, augmented with a 24 MeV elastic-scattering distribution from the literature, is used to develop two phenomenological optical-statistical models, both of which describe the data very well. First, the parameters of the conventional spherical optical model (SOM) are deduced. Second, the model in which the dispersion relationship, linking real and imaginary interactions (DOM), is considered. The SOM parameters are consistent with systematics previously reported from this laboratory, and the volume integral per nucleon of the real potential strength, J_V, and the radius, r_V, are energy dependent. Although the energy dependence of J_V is reduced by about 30% in going from the SOM to the DOM, there is little change in the E variation of r_V between the two models. Both models are extrapolated to the bound-state regime where they have modest success in predicting the binding energies of the single-particle and single-hole states in ^{90}Zr.

PACS number(s): 25.40.Dn, 25.40.Fq, 24.10.Ht, 27.50.+e

I. INTRODUCTION

The total and elastic-scattering cross sections of fast neutrons from nuclei are generally described in terms of an optical model having real, imaginary, and spin-orbit components. For spherical nuclei, there are two variants of this model in vogue at present. The first is the spherical optical model (SOM) with a real Woods-Saxon potential, an imaginary surface-peaked derivative Woods-Saxon well with perhaps a volume absorption setting in at energies of $\gtrsim 20$ MeV, and a spin-orbit potential of the Thomas form [1]. In the second formulation the fundamental dispersion relationship [2] linking the real and imaginary optical-model potentials is taken into account. This will be referred to as the dispersive optical model (DOM). In this paper parameters defining both a SOM and a DOM describing neutron scattering from elemental zirconium are deduced. To apply this model to specific isotopes one must know the magnitude and sign of the $(N-Z)/A$ lane term of the potentials [3]. This cannot be determined from our elemental data, but can be deduced from the Ohio University isotopic zirconium studies [4,5]. It should be noted that the coefficient of the $(N-Z)/A$ term extracted from the Ohio data has the opposite sign for the imaginary potential than that given by global models [6,7]. This sign is, however, consistent with the results of 8-MeV cross-section ratio measurements made on adjacent nuclei at this laboratory [8], and with the fact that the imaginary potential increases rapidly as one moves away from a closed shell [9].

Since we consider the differential elastic scattering between ≈ 1.5 and 24 MeV and the total cross sections from thermal to 20 MeV, the energy variation of the model parameters is reasonably defined over a wide range. As both the SOM and the DOM are fitted to the same data, we can check the conjecture [10] that the energy dependence of the geometric model parameters of the real SOM are due entirely to the fact that the dispersion contribution to the real potential was neglected—a conjecture the present work does not support. Furthermore, as discussed by Mahaux and collaborators [11–13], once the energy variation of the optical-model parameters is known, one can use the dispersion relationship to extrapolate to the bound-state regime; that is, deduce the shell-model potential. Combining this result with the $(N-Z)/A$ dependence, one can examine the neutron binding energies of the single-particle and single-hole states of the closed-shell nucleus ^{90}Zr.

In Sec. II the experimental procedures used in the measurements are outlined. In Sec. III the experimental results are presented. Sections IV and V are devoted to the determination of the parameters of the SOM and the DOM, respectively, and to comparing their theoretical predictions with the experimental results. The predicted binding energies of the neutron single-particle and single-hole states in ^{90}Zr are discussed for both the SOM and the DOM in Sec. VI. Finally, in Sec. VII our results are summarized and discussed.[†]

II. EXPERIMENTAL PROCEDURES

All of the measurements were made using the pulsed-beam fast-neutron time-of-flight technique. The neutron angular distributions were determined using the Argonne

---

*Visiting scientist from Japan Atomic Energy Research Institute, Tokai Establishment, Tokai-mura, Japan.

[†] A detailed description of this work is given in the Argonne National Laboratory Report ANL/NDM-119, 1991.

10-angle time-of-flight apparatus with flight paths of ≈ 5 m [14,15]. Higher-resolution measurements were made at selected energies using a heavily shielded 14.52-m flight path at a scattering angle of 80° [16].

The scattering samples were solid metal cylinders of elemental zirconium 2 cm in diameter and 2 cm long. The chemical purity of the samples was $>99\%$. Below 4 MeV, reference standard samples of carbon (pile grade graphite) were used, and above 4 MeV the reference standard was hydrogen in the form of polyethylene (CH_2). The standard samples were the same dimensions as the zirconium ones, and of better than 99% chemical purity. The weights of all the samples were measured to an accuracy of better than 0.01% using conventional techniques.

Below 4 MeV the $^7Li(p,n)$ source reaction [17] was used, with the lithium metal vacuum evaporated onto tantalum backings to thicknesses giving neutron energy spreads of $\approx 50-70$ keV at a 0° source-reaction angle. Above 4 MeV the $^2H(d,n)$ reaction [17] was used, with the deuterium gas contained in a cell ≈ 2 cm long. The deuterium gas pressure within the cell was adjusted to give neutron energy spreads of ≈ 250 keV at 4.5 MeV, decreasing to ≈ 125 keV at 10 MeV at 0°. The mean energy of the neutron sources was determined to $\lesssim 20$ keV by magnetic analysis of the incident charged-particle beam. The neutron sources were pulsed at a repetition rate of 2 MHz, with a burst duration of ≈ 1 nsec.

The scattering samples were placed ≈ 17 cm from the neutron source at 0° reaction angle. In the angular-distribution measurements, a massive collimator system defined the ten approximately 5-m flight paths, distributed over scattering angles between 18° and 160°. The relative angular scale of the scattering apparatus was determined to 0.05° using optical instruments. Below an incident energy of 4 MeV, the zero of this angular scale was determined to $\approx 0.2°$ using optical methods. Above 4 MeV, the zero for the angular scale was determined to better than 0.15° by the observation of neutrons scattered from a relatively heavy target both right and left of the apparent center line, over a forward angular range where the elastic scattering from the sample is very rapidly changing with angle. In the higher-resolution long-flight-path measurements, the neutron source and sample were surrounded by a massive concrete shield ≈ 1.5 m thick. The interior of this shield was a room ≈ 2.5 m on a side, lined with polyethylene, cadmium, and boron in order to reduce backscattering to the sample position. A precision collimator penetrated this shielded vault at an 80° scattering angle.

The neutron detectors used in the angular-distribution measurements were organic liquid scintillators 2 cm thick and 12.5 cm in diameter. Their γ-ray response was suppressed using pulse-shape-sensitive techniques. Similar scintillators were used for the long-flight-path higher-resolution measurements, but they were larger (5 cm in thickness and 25 cm in diameter), and four of them were arranged in a square array. This array was then placed within a heavy concrete shield approximately 1 m thick in order to suppress the ambient background. The relative energy dependence of the efficiency of each detector was determined by the observation of neutrons emitted in the spontaneous fission of ^{252}Cf, as described in Ref. [18]. These relative detector efficiencies were then normalized to either hydrogen or carbon reference standards [19] by observing either differential elastic scattering from polyethylene (for measurements >4 MeV) or the total cross section of carbon as described in Ref. [20] (for measurements <4 MeV).

The incoming experimental information was sorted and stored in a digital computer, and then reduced to cross sections using a complex data-processing system that has been developed over many years [21]. A part of this system includes Monte Carlo corrections for multiple-event, angular-resolution, and beam-attenuation effects [22].

III. EXPERIMENTAL RESULTS

A. Elastic neutron scattering

At energies of a few MeV, the elastic-scattering cross sections of zirconium may fluctuate with energy due to residual resonance effects. Therefore, at energies below 4 MeV the elastic-scattering measurements were taken in considerable energy detail. The scattered-neutron resolution was sufficient to separate the elastic and inelastic contributions. The angular distributions were measured at $\approx 70-100$-keV intervals from ≈ 1.5 to 3.0 MeV. At these lower energies, and with the broad incident-energy spreads, the observed angular distributions do not display a great deal of structure, so they were reasonably defined by ten differential measurements at each incident energy, distributed between $\approx 25°$ and 155° (distributions obtained with small incident-energy spreads fluctuate by large amounts as the individual resonances become apparent). From 3 to 4 MeV, the elastic-scattering distributions were measured at ≈ 200-keV incident-energy intervals, with 20 differential values per distribution. The total uncertainties in the individual differential values (including counting statistics, angular uncertainties, correction factors, and normalizations) were estimated to be $\leq 5\%$. These lower-energy results were obtained at this laboratory some time ago, and are discussed in more detail in Ref. [23].

Above 4 MeV, the measurements were made at approximately 0.5-MeV intervals from 4.5 to 10.0 MeV, and the angular range was $\approx 18°$ to 160°. The data were taken over a several-year period in sets of 20–40 angular values at each measurement period and incident energy. When combined, the average number of differential values per distribution was 107, sufficient to give good definition of the angle-dependent structure. Throughout the measurements, the scattered-neutron resolution was sufficient to reasonably resolve the elastic and inelastic contributions. In a number of ways (e.g., angular scale, detector normalizations, etc.) the measurements at the various experimental periods were independent; thus, reproducibility is some indicator of reliability. The uncertainties associated with the differential values varied a great deal depending on the care given a particular measurement and on the scattering angle. Except at the very minima of the distributions, statistical uncertainties were relatively small

($\leq 1-3\,\%$), as were those associated with the Monte Carlo correction procedures ($\leq 1\%$). The reference $\mathrm{H}(n,n)$ scattering standard is known to better than 1%. The detector calibration procedures were complex, and it is difficult to quantify the uncertainties associated with them. A subjective estimate is $\lesssim 3\%$ below 8 MeV and $<5\%$ at higher energies. The above elastic-scattering results are illustrated in Fig. 1. Some isotopic elastic-scattering results have been reported, and these will be compared with the present measurements in Sec. IV.

B. Inelastic neutron scattering

At lower energies, the broad resolution required for a reasonable energy averaging of fluctuations precludes optimum resolution of the inelastically scattered neutron groups. Moreover, the element consists of four isotopes of significant abundance, resulting in a large elemental level density and thus very complex inelastically scattered neutron spectra. Despite this, the discrete inelastic-scattering cross sections were determined at incident energies of less than 4 MeV, and the results largely consisted of the composite contributions from the excitation of levels in several isotopes. Nine such "elemental" inelastic groups were identified and attributed to the excited levels as given in Table I. The corresponding angle-integrated inelastic-scattering cross sections of the first five of these groups, shown in Fig. 2, were obtained by fitting the measured differential cross sections with second-order Legendre-polynomial expansions. The illustrated errors are larger than for elastic scattering due to lower counting rates and to uncertainties in the experimental resolution of the underlying complex structures. There have been remarkably few measured discrete inelastic-scattering cross sections of elemental zirconium reported, doubtless because of the experimental difficulties outlined above. There have been some isotopic results, and these are discussed and compared with the present work in Sec. IV.

Above 4-MeV incident-neutron energy, the inelastically scattered neutron spectrum blends into a continuum upon which is superimposed some small structure due to clumping of neutron groups from levels in the various isotopes. Spectra obtained with the 5-m flight paths displayed only a trace of the excitation of the 941-keV "level" observed at lower energies. The contribution was generally a very small artifact on the shoulder of the much larger elastic-scattering peak. Therefore, no attempt was made to deduce the corresponding cross sections from the 5-m measurements. There were two prominent structures in the 5-m spectra, one corresponding to excitations of $\approx 1.85-2.2$ MeV and the other to excita-

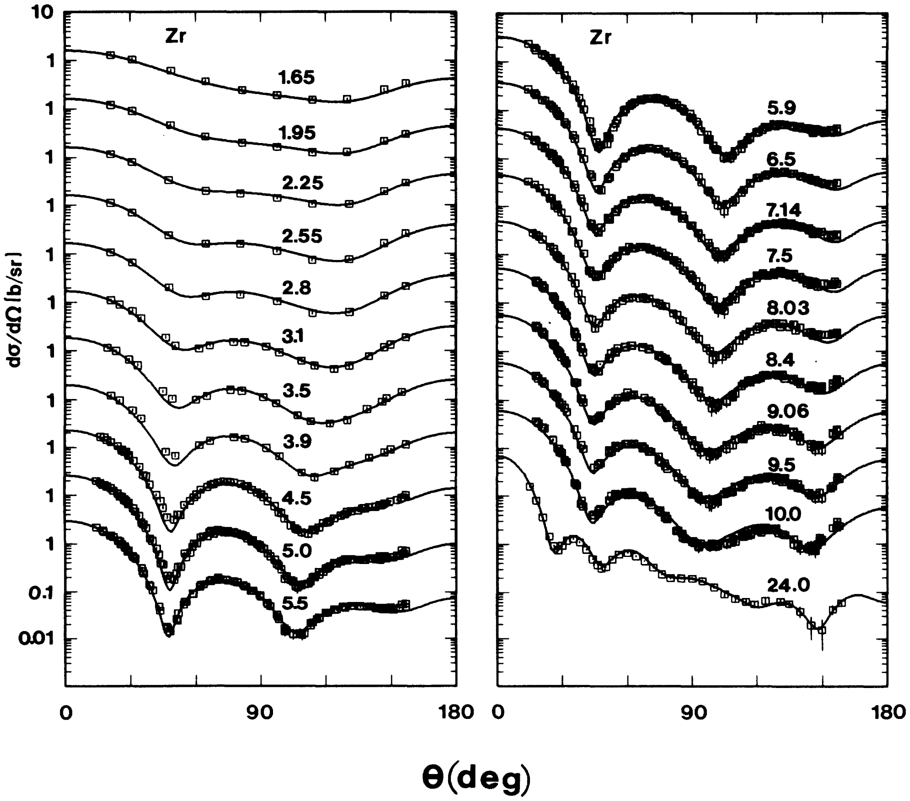

FIG. 1. Measured and calculated elastic-scattering cross sections of elemental zirconium. The measured data are indicated by □ symbols, where all results for $E \leq 10$ MeV are from the present work and the 24-MeV distribution is from Ref. [5]. The results of SOM calculations are indicated by curves. Incident energies are given numerically in MeV. The data are in the laboratory coordinate system.

TABLE I. Discrete inelastic-neutron excitation energies of elemental zirconium (in keV) at incident energies of less than 4 MeV.

No.	Exp.	Excitation energies ^{90}Zr[a]	^{91}Zr[a]	^{92}Zr[a]	^{94}Zr[a]
1	941±25	. . .	. . .	934(2+)	919(2+)
2	1476±37	. . .	1205($\frac{1}{2}$+)	1383(0+)	1300(0+)
			1466($\frac{5}{2}$+)	1495(4+)	1470(4+)
3	1787±23	1761(0+)	1882($\frac{7}{2}$+)	1847(2+)	1671(2+)
4	2101±26	. . .	2042($\frac{3}{2}$+)	2067(2+)	2058(3−)
			2131($\frac{9}{2}$+)		
5	2221±17	2187(2+)	many	2150(?)	2151(2+)
6	2363±14	2319(5−)		many	many
7	2791±15	2739(4−)		many	many
		2750(3−)			
8	3101±25	3077(4+)		many	many
9	3331±?	3309(2+)		many	many

[a] Nuclear Data Sheets as given in Refs. [24–27].

tions of ≈2.6–2.9 MeV. The corresponding emitted-neutron distributions were essentially isotropic, and the angle-integrated cross sections, given in Table II, were obtained assuming isotropy.

The 14.5-m measurements were limited to one scattering angle, 80°, but gave superior energy resolution. Superimposed on the neutron continuum some neutron groups stood out, and assuming isotropy of emission, their cross sections are given in Table II. The measured cross section for the first 941-keV "level" is more than an

TABLE II. Comparisons of measured and calculated compound-nucleus inelastic-scattering cross sections as discussed in the text.

$\bar{E}_x \approx 0.941$ MeV

E_{in} (MeV)	14.5-m flight path $d\sigma/d\Omega$ (mb/sr)	σ (mb)	CN cal.[a] σ (mb)
6.0	2.6	32.7	2.2
7.0	2.9	36.4	0.6
8.0	2.5	31.4	0.2

$\bar{E}_x \approx (1.85\text{–}2.2)$ MeV

E_{in} (MeV)	Flight path 5 m σ (mb)	14.5 m $d\sigma/d\Omega$ (mb/sr)	σ (mb)	CN cal. σ (mb)
4.5	321			307
5.0	235			233
5.5	163			178
6.0	125	11.9	150	137
6.5	107			103
7.0	83	4.6	58	82
8.0		4.4	55	49

$\bar{E}_x \approx (2.6\text{–}2.9)$ MeV

E_{in} (MeV)	Flight path 5 m σ (mb)	14.5 m $d\sigma/d\Omega$ (mb/sr)	σ (mb)	CN cal. σ (mb)
5.5	147			162
6.0	133	12.7	160	139
6.5	103			107
7.0	95	5.8	73	85
8.0		3.4	43	53
8.4	54			42

[a] CN denotes compound-nucleus calculations.

order of magnitude larger than the compound-nucleus prediction. Thus a strong direct-reaction component must be present (see Sec. IV) and the isotropy assumption, leading to the numerical values of Table II, is not valid. Two other "levels" evident in the long-flight-path results corresponded to the ≈1.85–2.2- and ≈2.6–2.9-MeV groups. Assuming isotropy, their respective cross sections are given in Table II. There is reasonable consistency between the results obtained with the two flight paths, and with the predictions of the compound-nucleus model (see Sec. IV), so that the assumption of isotropy is reasonable. The uncertainties associated with the measured 14.5-m flight-path values in Table II are estimated to be ≈10%, with a larger value for the 0.941-keV level due to its very small cross sections and probable anisotropy.

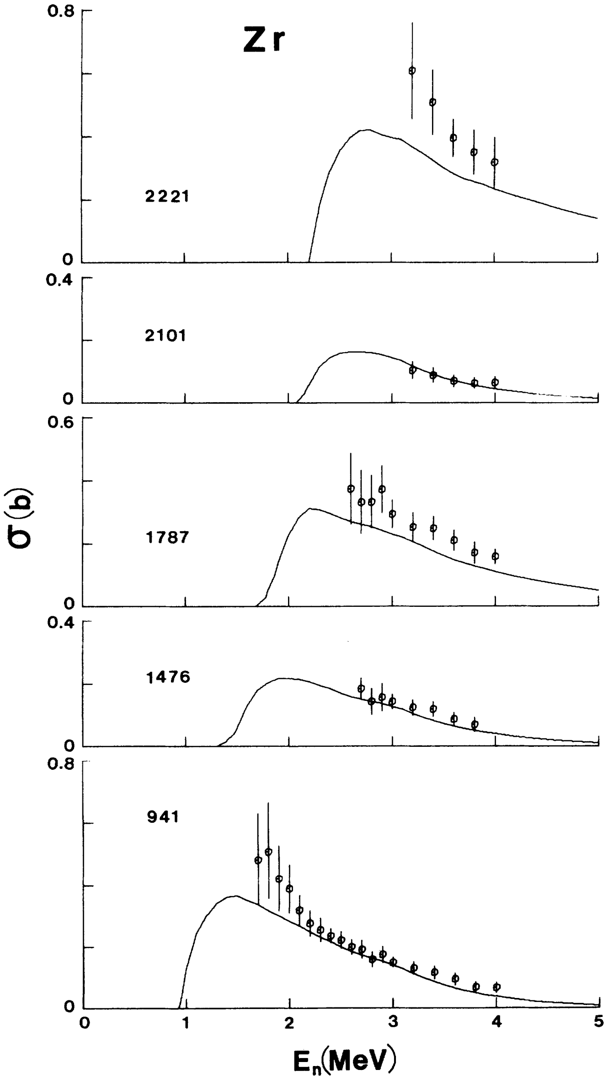

FIG. 2. Cross sections for the excitation of elemental "levels" in zirconium. Symbols indicate the present experimental results and curves the calculated values as discussed in Sec. IV of the text. Observed excitation energies are given in keV.

IV. PHENOMENOLOGICAL OPTICAL-STATISTICAL MODEL

This portion of the interpretation is based upon the conventional SOM [1], and is complicated by the multi-isotopic nature of the elemental samples used in the measurements. More than half of the element consists of ^{90}Zr (51.45%), and the remaining isotopes are ^{91}Zr (11.27%), ^{92}Zr (17.17%), ^{94}Zr (17.33%), and ^{96}Zr (2.78%) [28]. In view of the very small elemental abundance of ^{96}Zr, it was ignored in the present analysis. The remaining four isotopes have quite different excited states, particularly ^{90}Zr, and thus each will have a different compound-elastic-scattering contribution. These differences, together with size and isospin effects, should be considered in the interpretation. In the present work a special version of the spherical optical-model code ABAREX was used [29]. This formulation of the code has the capability to χ^2 fit the experimental observables, explicitly treating the individual direct and compound-nucleus contributions from up to ten isotopes, and combining them to obtain the elemental result directly comparable with experiment. The excitation of the discrete levels, as well as the statistical level properties, of each of the contributing isotopes were explicitly treated in the fitting. Compound-nucleus processes were calculated using the Hauser-Feshbach theory [30], as corrected for resonance width fluctuation and correlation effects by Moldauer [31].

The primary database for the derivation of the model parameters consisted of the present elastic-scattering results extending from ≈1.5 to 10 MeV (Fig. 1). Elastic scattering at energies of less than 1.5 MeV was not considered since fluctuations in the cross sections, primarily due to the prominent closed-shell ^{90}Zr isotope, make the results suspect in the sense that they are not consistent with the energy-average concept of the SOM. To guard against such fluctuations above 1.5 MeV, the database was averaged over ≈200-keV incident-energy intervals up to 4 MeV. Above 10 MeV, only one set of good quality differential elastic-scattering cross sections was found in the literature, the 24-MeV distributions of Ref. [5]. The latter results are isotopic, but from them an elemental distribution was constructed. It was added to the primary database to give a higher-energy elastic-scattering distribution for the fitting. This database was χ^2 fitted, as described in Ref. [32], to determine the SOM parameters. The analysis also gave consideration to the elemental neutron total cross section, as summarized in Ref. [33], and to the isotopic *s*- and *p*-wave strength functions, though these observables were not a part of the χ^2 fitting procedure.

All the discrete levels [24–27] below 4 MeV in ^{90}Zr and below 3 MeV in ^{91}Zr, ^{92}Zr, and ^{94}Zr were taken into account in these calculations. Although most of them have known J^π values, there were a few cases where ambiguity existed. However, these were all at a fairly high excitation energy, where many exit channels are open, so that the calculated results are not very sensitive to the assumed J^π estimates. The effect of compound-nucleus processes involving excitations above the discrete levels was calculated using the statistical level representation of

Gilbert and Cameron [34]. The temperatures, E_0 values, and spin cutoff factors used in the calculations are given in Ref. [32]. They provide a reasonable extrapolation to the known discrete level structure, and modest variations in them did not significantly change the results of the fitting.

The SOM was assumed to have Woods-Saxon and derivative Woods-Saxon forms for the real and imaginary potentials, respectively, and a Thomas spin-orbit term [1]. Although the neutron polarization data are sensitive to the spin-orbit potential, the Zr elastic-scattering cross-section data are not. Since comprehensive polarization data is not available for zirconium, the choice of this interaction is, within reason, rather arbitrary. Throughout most of the present analysis, it was assumed that

$$\begin{aligned} V_{\mathrm{s.o.}} &= 5.5\ \mathrm{MeV}\ , \\ r_{\mathrm{s.o.}} &= 1.005\ \mathrm{fm}\ , \\ a_{\mathrm{s.o.}} &= 0.65\ \mathrm{fm}\ . \end{aligned} \tag{1}$$

These parameters are similar to those given in global SOM's deduced when polarization data were available [6]. (Throughout this paper radii are expressed in the form $R_i = r_i A^{1/3}$.)

The effect of the isovector interaction, the $(N-Z)/A$ term [3], would be to decrease the real and imaginary strengths by about 1.2% and 7.4%, respectively, in going from ^{90}Zr to ^{94}Zr if, for example, the global 10-MeV parameters of Walter and Guss [6] are used. Such changes were examined and found to have little impact, and hence were neglected in the subsequent analysis. In addition, even though the database extended to 24 MeV, no evidence for any significant volume absorption was found. This result is in agreement with the findings of Wang and Rapaport [5].

The details of the SOM parameter search, first determining the real potential geometry, then the imaginary-well geometry, and finally the potential strengths, are given in Ref. [32]. The strengths were expressed as volume integrals per nucleon, J_i, where

$$J_i = \frac{4\pi}{A} \int_0^\infty V_i(r) r^2 dr\ . \tag{2}$$

The values of J_V and J_S, shown in Fig. 3, were deduced from the strengths and geometries of the optical-model potentials assuming that $A = 91.3$ (i.e., the weighted average for the elemental sample). From Fig. 3, it is clear that the J values resulting from the fitting varied in an approximately linear manner with energy. The uncertainties in these J_i values are related in a complex manner to the model interpretation and the underlying data. For J_V they were estimated to be 1.5% above 4 MeV and 2% below 4 MeV, whereas for J_S these estimates become 5 and 10%, respectively. An error weighted least-squares fit to the values shown in Fig. 3 gives the results quoted in Table III where the geometric parameters of the SOM are also tabulated.

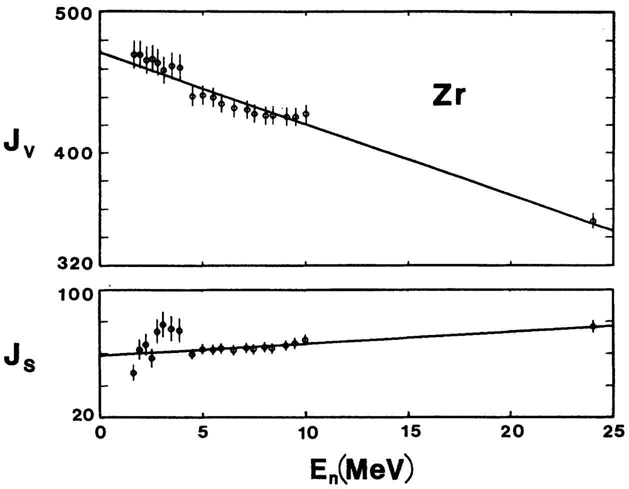

FIG. 3. Real (J_V) and imaginary (J_S) volume integrals per nucleon as a function of incident energy for the SOM. Experimentally deduced values are indicated by symbols, and the straight lines indicate the results of weighted fits given in Table III. The J_i units are MeV fm^3.

The results calculated with the SOM are compared with the experimental data from which it was developed in Fig. 1, and the agreement is generally very good. The same model gives a good description of the elemental zirconium neutron total cross section from a few keV to at least 20 MeV as illustrated in Fig. 4. The measured and calculated values agree to within several percent over the entire energy range.

To apply this model to the data observed for the various zirconium isotopes, one must make some assumption about the $(N-Z)/A$ dependence of the deduced potentials. For this purpose, we assume that J_V can be expressed in the form

$$J_V = J_0[1 + \alpha_V (N-Z)/A] + \beta_V E\ , \tag{3}$$

with J_0 and α_V independent of energy, and β_V independent of $(N-Z)/A$. The global models of Walter and Guss [6] and of Rapaport [7] give $\alpha_V = -0.31$ and -0.42, respectively. The fitting of the separated isotopic data [5] at 8, 10, and 24 MeV leads to $\alpha_V = -0.35$, and we shall use this value. In order that J_V has the value given in Table III when $Z = 40$, $N = 51.3$, and $A = 91.3$ it follows that

TABLE III. Comparison of SOM and DOM optical-model parameters.

SOM	DOM
Real potential	
$J_V = 471.17 - 5.09E$	$J_{\mathrm{eff}} = 455.6 - 3.41E$ MeV fm^3
$r_V = 1.310 - 0.0063E$	$= 1.300 - 0.0054E$ fm
$a_V = 0.667$	$= 0.685$ fm
Imaginary potential	
$J_S = 58.36 + 0.74E$	$J_S = 60.59 + 0.58E$ MeV fm^3
$r_W = 1.390 - 0.0063E$	$= 1.385 - 0.0071E$ fm
$a_W = 0.310 + 0.0180E$	$= 0.255 + 0.0253E$ fm

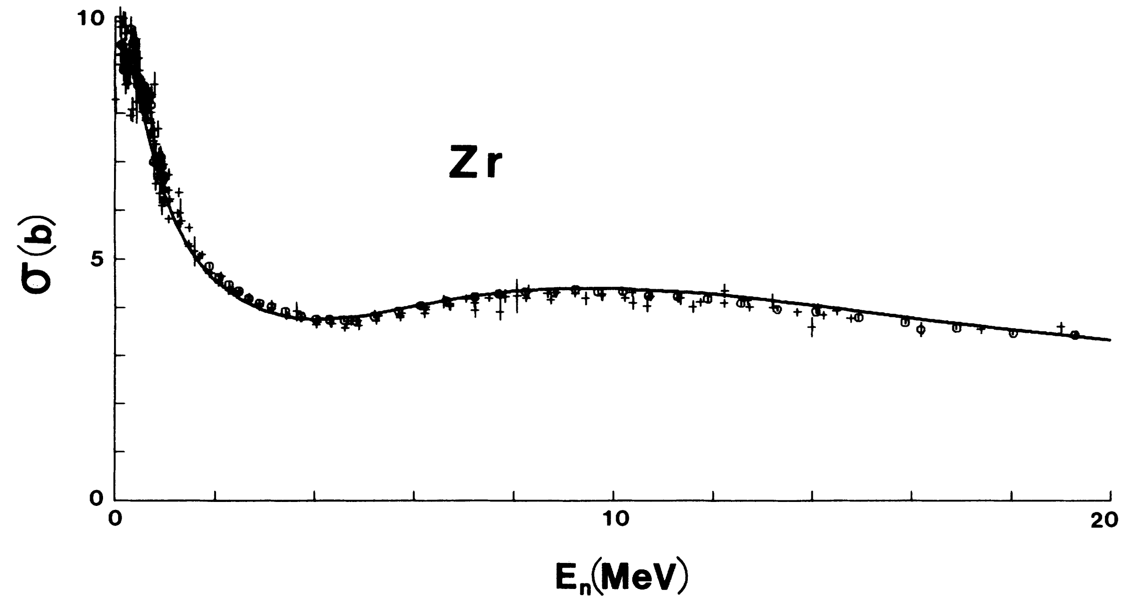

FIG. 4. Comparison of measured (symbols) and SOM calculated (curve) neutron total cross sections of elemental zirconium. The various experimental values are taken from the literature as described in Refs. [32,33].

$$J_V = \{492.50[1-0.35(N-Z)/A]-5.09E\}\ \text{MeV fm}^3 . \quad (4)$$

A similar expression can be written for J_S. According to the global models [6,7], α_S is negative and has an absolute magnitude greater than unity. On the other hand, the zirconium isotopic data [5] clearly indicates that the value of J_S increases with increasing $(N-Z)/A$—in

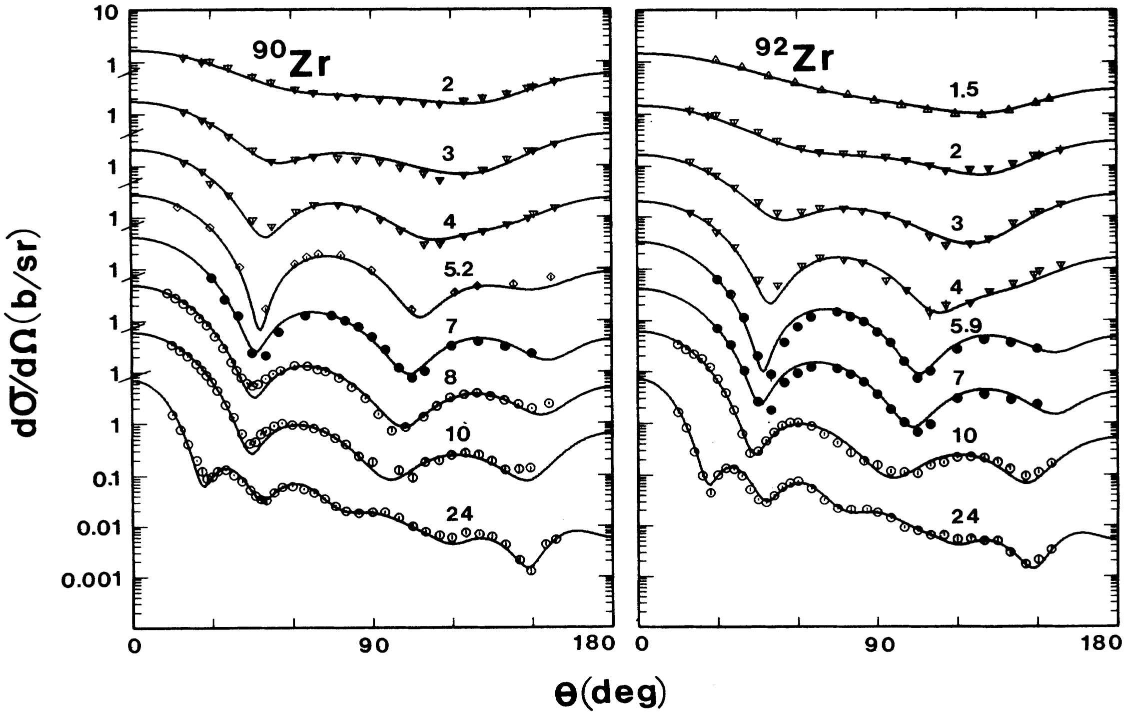

FIG. 5. Comparison of measured (symbols) and SOM calculated (curves) differential elastic-scattering cross sections of ^{90}Zr and ^{92}Zr. The measured values were taken from Refs. [5,32,36,37]. Incident energies are numerically given in MeV. The data are given in the laboratory coordinate system.

other words, the sign is opposite to that given by the global models. This is understandable since ^{90}Zr has 50 neutrons, and it is well known that J_S increases rapidly as one moves away from a closed shell [9]. Physically, J_S is a measure of the softness (ease of excitation) of the core, and it is well known that closed-shell nuclei, such as ^{90}Zr, have stiffer cores; i.e., fewer low-lying states with smaller excitation probability. Thus, for these nuclei a smaller absorption potential is needed. The Zr isotopic data of Wang and Rapaport [5] indicate that α_S could be as large as 5–10. However, in view of the uncertainties in the data and in the derivation of the model from the data, we feel a more realistic estimate of α_S is probably about 2. Accepting this, in order that J_S have the values given in Table III for $Z=40$, $N=51.3$, and $A=91.3$, one finds that

$$J_S=\{46.78[1+2(N-Z)/A]+0.74E\}\ \mathrm{MeV\,fm}^3\ . \qquad (5)$$

The low-energy strength functions deduced from resonance measurements were not a part of the database used in the fitting. However, the calculated values, using the geometries of Table III and the potential strengths given by Eqs. (4) and (5), are in reasonable agreement with those deduced from resonance measurements [35], as listed in Table IV. The predicted s-wave strength function decreases slightly as one goes to the heavier isotopes, and the p-wave values increase. Although the experimentally derived data has a great deal of scatter, it does exhibit the same general mass-dependent trends. Of course, since the model has only a smooth dependence on $(N-Z)/A$, it cannot reproduce the fluctuations evident in the experimentally based data which may reflect detailed differences in nuclear structure, small resonance samples, or other experimental uncertainties. The calculated scattering length R' decreases from 6.95 fm for ^{90}Zr to 6.86 fm for ^{96}Zr and is in reasonable agreement with the experimentally deduced value [35] of 7.2±0.2 fm for all the isotopes.

In Figs. 5 and 6 the predictions of the model, with the

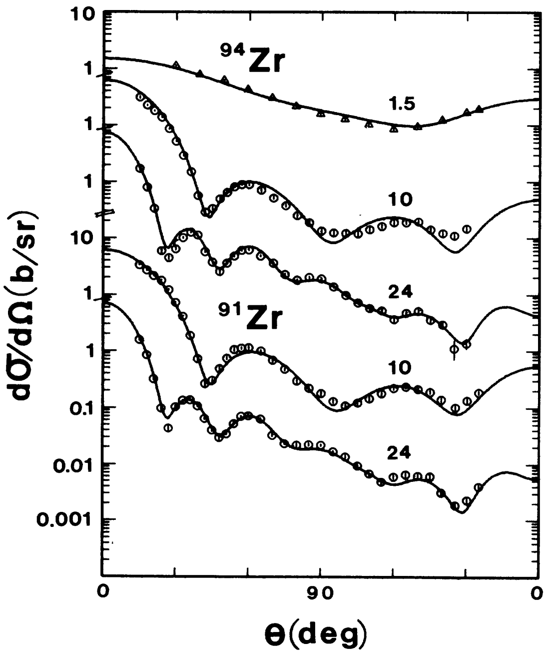

FIG. 6. Comparisons of measured (symbols) and SOM calculated (curves) differential elastic-scattering cross sections of ^{91}Zr and ^{94}Zr. The measured values were taken from Refs. [5,38]. Incident energies are numerically given in MeV. The data are given in the laboratory coordinate system.

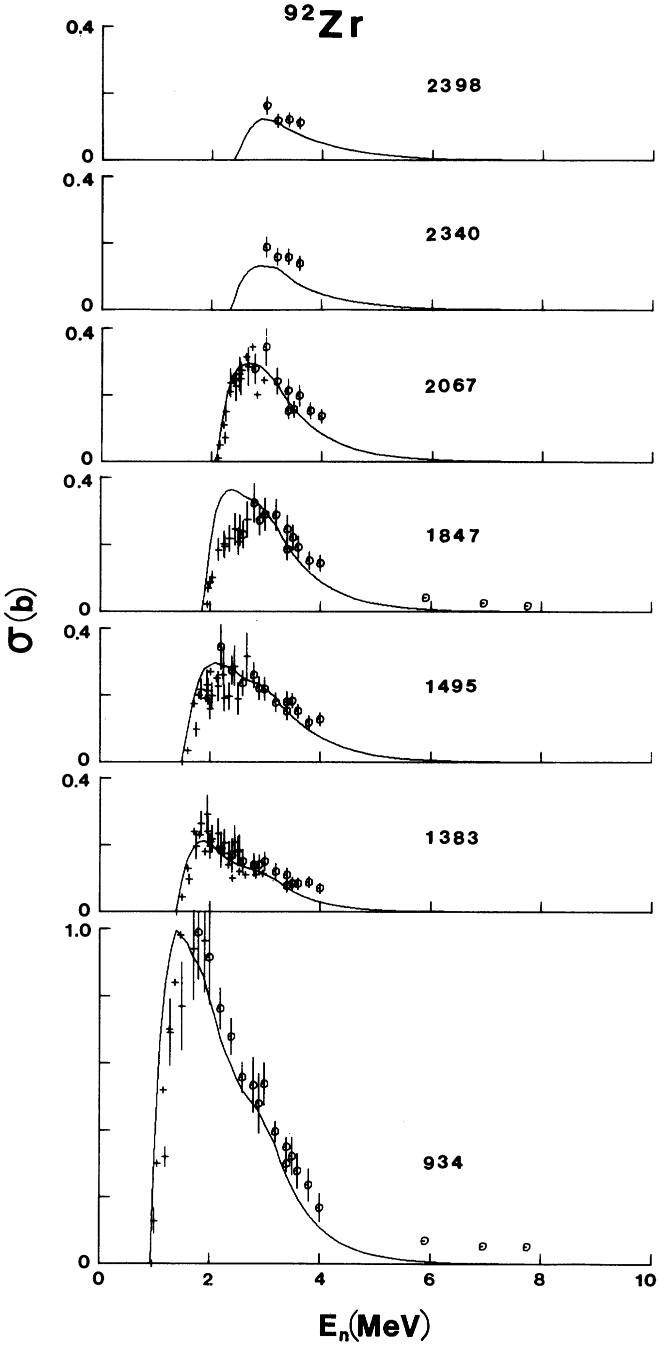

FIG. 7. Illustrative comparisons of measured (symbols) and SOM calculated (curves) cross sections for the excitation of specific levels in ^{92}Zr. The notation is identical to that of Fig. 2. The measured values are taken from the literature as described in Refs. [32,33].

potential strengths of Eqs. (4) and (5), are compared with experiment. The data for the two isotopes ^{90}Zr and ^{92}Zr are reasonably extensive [5,33,36,37], and agreement between measured and calculated results is remarkably good from 1.5 to 24 MeV, as illustrated in Fig. 5. The experimental data [5,38] for ^{91}Zr and ^{94}Zr are less comprehensive, but again the model appears reasonably suitable, as shown in Fig. 6.

It is difficult to relate observed elemental inelastic-scattering cross sections to the excitation of specific levels in individual isotopes. However, there is some isotopic inelastic-scattering information reported in the literature, and summarized in Ref. [33], which is primarily confined to inelastic scattering from ^{90}Zr and ^{92}Zr. Some of these ^{92}Zr experimental results are compared with the predictions of the model in Fig. 7, and similar ^{90}Zr comparisons are given in Ref. [32]. Given the experimental uncertainties, the agreement is acceptable. The calculated results are also compared with the present elemental measurements in Fig. 2. The agreement between the first few measured and calculated excitations is reasonably good at the low energies where the processes are primarily due to compound-nucleus reactions, but the complex elemental level structure makes comparisons for the higher-energy excitations less reliable. At higher energies, the inelastic scattering is observed as essentially a continuum distribution upon which is superimposed some structure due to clumps of levels. The measured composite inelastic-scattering cross sections are summarized in Table II. The inelastic-scattering cross sections implied by the two prominent scattered-neutron groups corresponding to observed excitations of ≈ 2.05 and 2.75 MeV are in good agreement with the predictions of compound-nucleus calculations using the SOM. However, the cross section at, for example, 8 MeV for the excitation of the 941-keV "level" is two orders of magnitude larger than predicted by compound-nucleus calculations. The observed excitation is primarily due to the yrast 2^+ levels in ^{92}Zr and ^{94}Zr, and these are known to have a strong direct-reaction component. For example, at 8 MeV the work of Wang and Rapaport [5] indicates similar 2^+ cross sections for ^{92}Zr and ^{94}Zr with a magnitude of ≈ 60 mb. Thus, the direct-reaction contributions of these two isotopes to the 941-keV level in elemental zirconium would be about 20 mb, and this is in reasonable agreement with the value given in Table II. Similar direct-reaction effects undoubtedly contribute to the higher-energy cross sections listed in that table, but their effects are not as dramatic as those of the 941-keV level, since in these cases the compound-nucleus cross section is ≈ 50 mb.

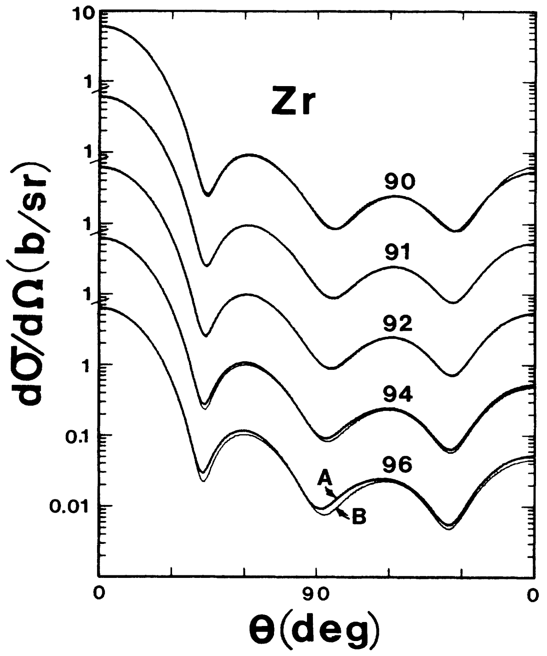

FIG. 8. The effect of the isovector potential on 10-MeV elastic scattering from the isotopes of zirconium. The heavy curves (A) were calculated using the same potential strengths given under SOM in Table III and taking into account the $R_i = r_i A^{1/3}$ size effect for each isotope. The light curve (B) included the $(N-Z)/A$ dependence of the potential strengths as given by Eqs. (4) and (5).

In fitting the elemental zirconium data the size dependence ($R_i = r_i A^{1/3}$) was taken into account, but the potential strengths were assumed to be the same for all constituents of the sample. The $(N-Z)/A$ dependence of the strengths was assumed to be unimportant and was ignored. We now return to quantitatively address this assumption. The darker curves (A) in Fig. 8 show the predicted 10-MeV elastic-scattering cross sections for the various isotopic constituents of elemental zirconium when the size variation is taken into account but the potential strengths, given in Table III (with $A = 91.3$) are assumed to be the same for each isotope. The lighter curves (B) show the effects of varying size and also in-

TABLE IV. Comparison of measured and SOM calculated strength functions ($\times 10^4$) for the isotopes of zirconium.

	s-wave strength function		*p*-wave strength function	
Isotope	Exp.[a]	Cal.	Exp.[a]	Cal.
^{90}Zr	0.7 ± 0.2	0.64	4.0 ± 0.6	5.19
^{91}Zr	0.36 ± 0.08	0.63	6.7 ± 1.3	5.45
^{92}Zr	0.50 ± 0.10	0.62	7.0 ± 1.3	5.69
^{94}Zr	0.50 ± 0.15	0.61	9.8 ± 2.0	6.10
^{96}Zr	0.34 ± 0.14	0.59	6.0 ± 1.8	6.40

[a] From Ref. [35].

clude the isovector component of the potentials—that is, take different strengths for each isotope deduced from Eqs. (4) and (5). For $A=91$ and 92 the two results are indistinguishable. For $A=90$ they differ only at very large angles where no data exist. Thus, for nearly 80% of the sample there is no experimentally accessible evidence of the $(N-Z)/A$ dependence of the potential. There are only slight differences between the two curves near the minima of the ^{94}Zr distribution, and these are smaller than the experimental uncertainties. It is only for ^{96}Zr that the differences are significant, and this isotope is less than 3% abundant. Thus, the assumption in the elemental fitting that the isovector effects could be ignored was valid.

V. THE DISPERSIVE OPTICAL MODEL

Since the foregoing analysis did not take into account the fundamental dispersion relationship [2], it is of interest to see what happens when this feature is incorporated.

The dispersion relationship links the real and imaginary OM potentials, or radial moments of these interactions, by the expression

$$V(r,E)=V_{\mathrm{HF}}(r,E)+\frac{\mathrm{P}}{\pi}\int_{-\infty}^{+\infty}\frac{W(r,E')dE'}{(E-E')}\ , \tag{6}$$

where $V(r,E)$ and $W(r,E)$ are the total real and imaginary potentials, respectively, $V_{\mathrm{HF}}(r,E)$ is the Hartree-Fock component, and P denotes the principal value integral. In the SOM, a derivative Woods-Saxon form was used for the imaginary potential, and this implies that the real interaction should have a surface component. In order to estimate the magnitude of this surface component, consider Eq. (6) expressed in terms of volume integrals per nucleon,

$$J_V(E)=J_{\mathrm{eff}}(E)+\frac{\mathrm{P}}{\pi}\int_{-\infty}^{+\infty}\frac{J_S(E')dE'}{(E-E')}\ . \tag{7}$$

In this expression $J_S(E)$ is the surface-peaked component of the imaginary potential, and $J_{\mathrm{eff}}(E)$ is the sum of the contribution due to $V_{\mathrm{HF}}(E)$ and any possible volume absorption. In order to evaluate the effect of the surface interaction on the real potential we define

$$\Delta J_S\equiv\frac{\mathrm{P}}{\pi}\int_{-\infty}^{+\infty}\frac{J_S(E')dE'}{(E-E')}\ , \tag{8}$$

where $J_S(E)$ must be known for all values of E. In order to estimate this quantity, $J_S(E)$ is assumed to be (i) symmetric about the Fermi energy E_F, where

$$\begin{aligned}E_F&=\tfrac{1}{2}(\epsilon_d+\epsilon_g)\\&=-9.6\ \mathrm{MeV}\ ,\end{aligned} \tag{9}$$

and ϵ_d and ϵ_g are the binding energies of the $d_{5/2}$ and $g_{9/2}^{-1}$ neutron states to the ^{90}Zr core. (ii) For $2E_F\le E\le 0$, $J_S=J_0(E-E_F)^2/E_F^2$, where $J_0=58.36$ MeV fm^3 is the value of J_S at $E=0$ (see Table III). (iii) For $0\le E\le 25$ MeV, J_S has the values given in Table III. (iv) For $E\ge 25$ MeV, J_S decreases linearly with energy to 0 at 60 MeV, and remains 0 at higher energies. With these assumptions, $\Delta J_S(E)$ was evaluated and is shown in the lower portion of Fig. 9. In the upper half of this figure the ratio

$$\lambda(E)=\Delta J_S(E)/J_S(E) \tag{10}$$

is shown, and it was assumed that this is the factor by which the imaginary potential should be multiplied to give the surface-peaked component of the real OM potential.

With the spin-orbit parameters held fixed to the values given by Eq. (1), a fit to the Zr elastic-scattering database, including the surface-peaked real component, was carried out in the same way as for the SOM, and the resulting parameters are listed under the heading DOM in Table III. The predictions for the elastic-scattering angular distributions and the total cross sections [33] obtained with this model agree very well with experiment, and are quite similar to the SOM results shown in Figs. 1 and 4. (The actual curves for these quantities obtained using the DOM are explicitly given in Ref. [32].) When the $(N-Z)/A$ dependences of the potential strengths, as given in Eqs. (4) and (5), are incorporated, the s- and p-wave strength functions deduced by use of the DOM are only a few-percent different from those given in Table IV, and this difference is considerably smaller than the uncer-

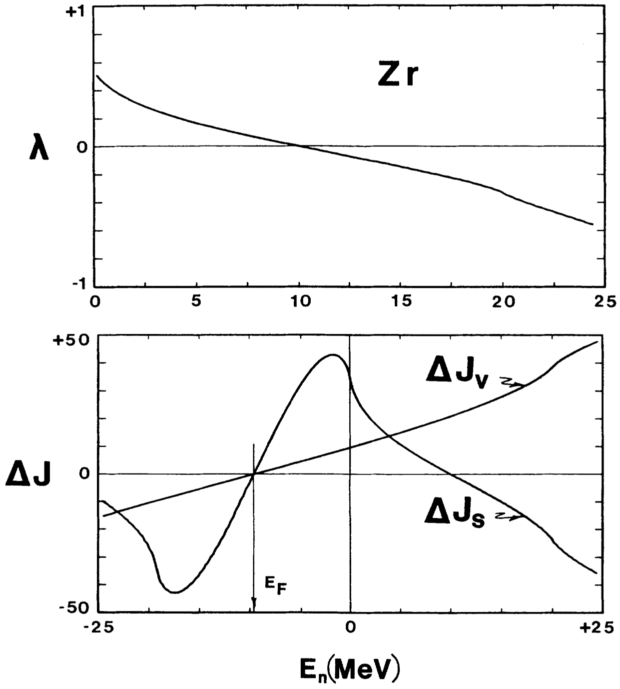

FIG. 9. The upper portion of the figure shows the λ factor of Eq. (10). The lower portion of the figure shows the volume integral per nucleon obtained for the surface potential ΔJ_S calculated using Eq. (8), and the assumptions directly following this equation. ΔJ_V, the possible addition due to volume absorption, was calculated using Eq. (12) with the magnitudes based on the assumptions discussed in the text.

tainties associated with the experimentally deduced values [35].

From a comparison of the SOM and DOM parameters given in Table III, it is clear that the inclusion of the surface real potential barely changes the E dependence of the geometrical parameters r_V, a_V, r_W, and a_W. Furthermore, the values of J_S are similar to those obtained using the SOM. This is fortunate since the value of $\lambda(E)$, Eq. (10), should have been calculated using the DOM imaginary potential, i.e., an iterative procedure should have been used. However, since J_S for the two models is so similar, a single iteration is sufficient. On the other hand, J_{eff} and J_V of the SOM are quite different, as they should be. Only when ΔJ_S, Eq. (8), is added to $J_{\text{eff}}(E)$ should the two be compared. In the positive energy range (0–25 MeV), $\Delta J_S(E)$, shown in Fig. 9, can be reasonably represented as a linear function of energy,

$$\Delta J_S = (25.6 - 2.1E)\ \text{MeV fm}^3 , \tag{11}$$

and when this expression is added to J_{eff}, a relationship quite similar to that describing J_V is obtained.

In the DOM fit to the data, J_{eff} is the sum of a Hartree-Fock component and a possible contribution from volume absorption. Since J_{HF} is expected to have a simple E dependence and J_{eff} is known experimentally to be almost linear in E for $E > 0$, it follows that ΔJ_V should be approximately a linear function of energy. To check this contention, and to estimate the magnitude of ΔJ_V, we assume that the volume absorption is symmetric about E_F, is zero for $0 \le E \le E_0$, increases linearly starting at E_0, attains a maximum value of J_m at $E = E_m$, and then is constant for all E greater than E_m. With these assumptions, ΔJ_V becomes

$$\begin{aligned}\Delta J_V(E) = \frac{J_m}{\pi(E_m - E_0)} \Bigg[& (E - E_0)\ln\left|\frac{E_m - E}{E_0 - E}\right| + (E_m - E_0)\ln\left|\frac{-2E_F + E_m + E}{E_m - E}\right| \\ & - (-2E_F + E_0 + E)\ln\left|\frac{-2E_F + E_0 + E}{-2E_F + E_m + E}\right| \Bigg] . \end{aligned} \tag{12}$$

If one, somewhat arbitrarily, takes $E_0 = 25$ MeV (the value of E at which the surface absorption was assumed to begin to decrease), $E_m = 60$ MeV (the value of E at which the surface absorption was assumed to reach zero), and $J_m = 76.86$ MeV fm^3 (the peak value of the SOM surface absorption according to Table III), then $\Delta J_V(E)$, shown in the lower portion of Fig. 9, is obtained. Over the energy range -25 to $+25$ MeV, it is clear that ΔJ_V is considerably smaller than J_{HF} and, moreover, is nearly a linear function of E,

$$\Delta J_V = 11.0 + 1.1E . \tag{13}$$

Thus, in the energy region of interest, J_{eff}, J_{HF}, and J_V are all approximately linear functions of E.

Although the spin-orbit parameters given in Eq. (1) are within the error bars of the values found in the analysis [39] of data on the neighboring nucleus ^{89}Y, the strength of this interaction is somewhat smaller than used in other analyses of data on the separated zirconium isotopes [4,5]. The effect of changing the spin-orbit potential to

$$\begin{aligned} V_{\text{s.o.}} &= (6.84 - 0.033E)\ \text{MeV} , \\ r_{\text{s.o.}} &= 1.14\ \text{fm} , \\ a_{\text{s.o.}} &= 0.5\ \text{fm} \end{aligned} \tag{14}$$

was examined by making a second DOM fit to the data. The parameters resulting from this fit are

$$\begin{aligned} J_{\text{eff}} &= (435.94 - 1.46E)\ \text{MeV fm}^3 , \\ r_V &= (1.2533 - 0.0007E)\ \text{fm} , \\ a_V &= 0.6839\ \text{fm} , \\ J_S &= (59.18 + 0.89E)\ \text{MeV fm}^3 , \\ r_W &= (1.3748 - 0.0048E)\ \text{fm} , \\ a_W &= (0.3419 + 0.0111E)\ \text{fm} . \end{aligned} \tag{15}$$

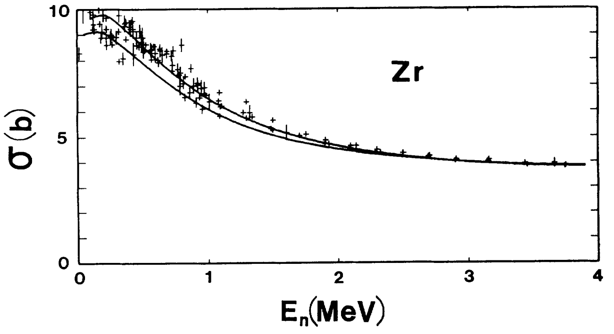

FIG. 10. Comparison of measured and calculated neutron total cross sections of zirconium. The upper curve was obtained with the DOM parameters of Table III and the spin-orbit interaction of Eq. (1). The lower curve was obtained using the DOM with the parameters of Eqs. (14) and (15).

A comparison of these DOM parameters with those of Table III shows that the changes are mainly in the real potential—the energy dependence of r_V has essentially vanished and that of J_{eff} has become quite small. The description of the elastic-scattering distributions is similar to that obtained with the spin-orbit potential of Eq. (1). However, the description of the neutron total cross section has markedly deteriorated at energies below about 4 MeV, and this is shown in Fig. 10 where the low-energy predictions for the two DOM's are plotted. Thus, a better overall description of the neutron interaction with zirconium is obtained with the DOM of Table III and the spin-orbit potential of Eq. (1).

VI. THE BOUND-STATE POTENTIAL

A. SOM

The dispersion relationship, Eq. (6), linking the real and imaginary potentials also relates the radial moments of these interactions,

$$\langle r(E)^q\rangle_V=\langle r(E)^q\rangle_{\mathrm{HF}}+\frac{\mathrm{P}}{\pi}\int_{-\infty}^{\infty}\frac{\langle r(E')^q\rangle_W}{E-E'}dE' , \tag{16}$$

where, for example,

$$\langle r(E)^q\rangle_W=\frac{4\pi}{A}\int_0^{\infty}r^qW(r,E)dr . \tag{17}$$

For ^{208}Pb, ^{89}Y, ^{51}V, and ^{40}Ca the $q=0.8$, 2, and 4 moments of the SOM potential [12,40–43] have been used to investigate the properties of the real interaction implied by Eq. (16) when $E<0$ (i.e., the shell-model potential which is assumed to be a Woods-Saxon well). In these calculations, the Brown-Rho [44] form for the radial moments of the imaginary potential was used,

$$\langle r(E)^q\rangle_W=\frac{C_q(E-E_F)^2}{(E-E_F)^2+D_q^2} , \tag{18}$$

so that $\langle r(E)^q\rangle_W$ was assumed to be symmetric about the Fermi energy E_F. Using the geometry of the imaginary well given in Table III, together with the 21 values of J_S shown in Fig. 3, radial moments for the above q values were calculated. The parameters C_q and D_q of Eq. (18) were then determined so as to give the best fit to these moments. No assumption was made about the form of the imaginary potential for $E>24$ MeV except that as $E\rightarrow\infty$ the various moments become constant and equal to the values C_q determined from the fit to the 0–24-MeV data.

Because of the simple form, Eq. (18), assumed for $\langle r(E)^q\rangle_W$, the principal value integral of Eq (16) can be carried out analytically. If one assumes that the Hartree-Fock contribution to $\langle r(E)^q\rangle_V$ has at most a linear dependence on E, Eq. (16) becomes

$$\langle r(E)^q\rangle_V=A_q+B_qE+\frac{C_qD_q(E-E_F)}{(E-E_F)^2+D_q^2} . \tag{19}$$

Using the geometry of the real well given in Table III, together with the J_V values of Fig. 3, the moments of the real potential, $\langle r(E)^q\rangle_V$, were calculated for $q=0.8$, 2, and 4. Using the previously determined C_q and D_q, the A_q and B_q of Eq. (19) were determined by least-squares fitting, and the values for the various coefficients are given in Ref. [32].

If one assumes that Eq. (19) for the three moments of the real potential also holds for negative energies, and if one takes a Woods-Saxon form for the interaction, values of the parameters $V_0(E)$, $r_V(E)$, and $a_V(E)$ needed to characterize the bound-state region, as well as the neutron-scattering potential, can be deduced. These are shown as a function energy in Fig. 11, together with the values of J_V, the volume integral per nucleon of this potential. J_V exhibits the characteristic Fermi surface anomaly and, as usual, this occurs at negative energies. The neutron-scattering values for r_V, a_V, and J_V, given in Table III, are shown as broken lines in the figure for $E\geq 0$. It is clear that the dispersion-obtained parameters of the Woods-Saxon well reproduce the positive-energy neutron-scattering results to good accuracy.

If one takes the shell-model spin-orbit strength as given by Eq. (1), this can be combined with the values of $V_0(E)$, $r_V(E)$, and $a_V(E)$, shown in Fig. 11, to predict the binding energies of the various single-particle and hole states in ^{90}Zr with the results shown under the heading "SOM" in Fig. 12. The figure also shows the experimental data under the heading "EXP." The energies of the $0g_{7/2}$, $1d_{3/2}$, $2s_{1/2}$, and $1d_{5/2}$ particle states were obtained by combining the ^{90}Zr$(d,p)^{91}$Zr data of Graue *et al.* [45] with the binding energy tables [46], and from this one concluded that they are bound by 4.4, 4.8, 5.5, and 7.1 MeV, respectively. The $0g_{9/2}$, $1p_{1/2}$, $1p_{3/2}$,

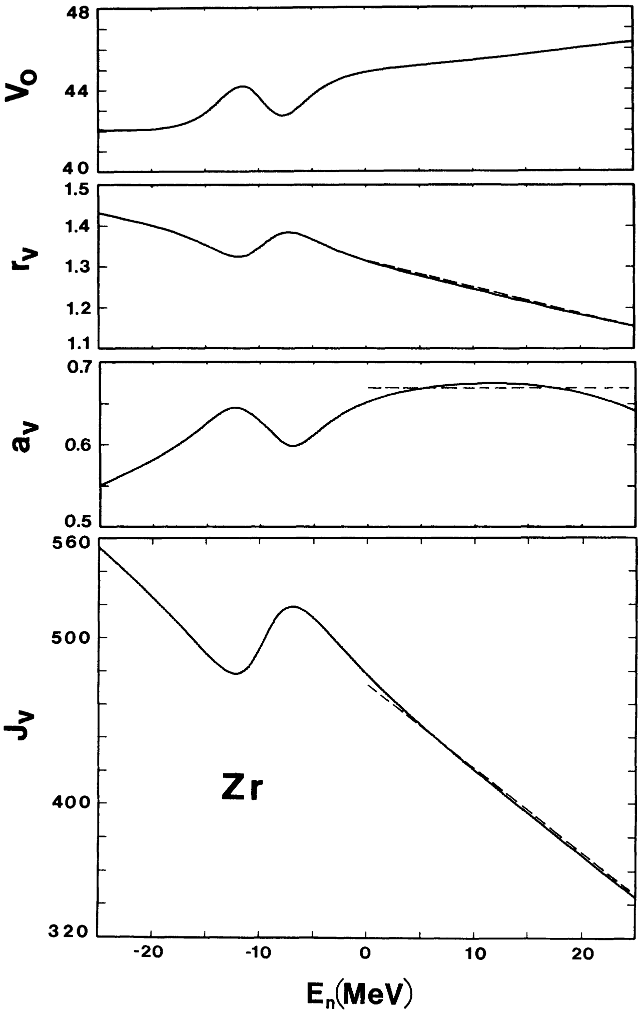

FIG. 11. The energy variation of V_0, r_V, and a_V characterizing the effective Woods-Saxon well deduced using Eq. (19) and the parameters given in Ref. [32]. For positive energies, the values given by a fit to the neutron-scattering data (see Table III) are shown as broken lines.

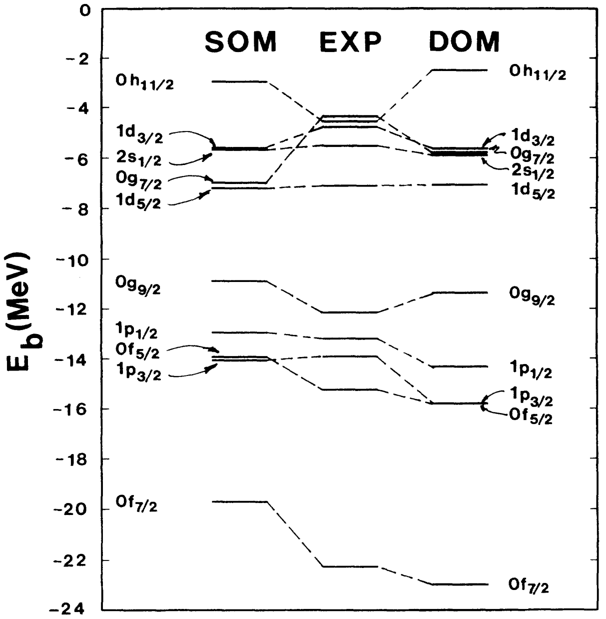

FIG. 12. Comparison of experimental (EXP) binding energies (E_b) of the particle and hole states in ^{90}Zr with model predictions. The SOM results were obtained with a Woods-Saxon well using the parameters shown in Fig. 11. The DOM results were obtained with the surface-peaked potential added to the Woods-Saxon well as described in the text, and the $E=0$ geometry given in Table III was used. The strength of the volume Woods-Saxon well was $J_V=(457.7-3.41E)$ MeV fm^3. In both cases the spin-orbit potential was of the Thomas form with the parameters of Eq. (1).

$0f_{5/2}$, and $0f_{7/2}$ hole-state energies can be obtained from the $^{90}\mathrm{Zr}(\vec{p},d)^{89}\mathrm{Zr}$ results of Kasagi *et al.* [47], and their data imply bindings of 12.1, 13.2, 13.9, 15.2, and 22.3 MeV for these states, respectively. Finally, one would expect the $0h_{11/2}$ level to come into binding in this region, and there is evidence for a large number of $l=5$ states in the stripping data. The center of gravity of these states can be calculated from a knowledge of the spectroscopic strength $\mathcal{S}_i$ to an $l=5$ state at energy E_i from the relationship

$$\epsilon=\sum_i \mathcal{S}_i E_i \Big/ \sum_n \mathcal{S}_n \; . \tag{20}$$

Using the known values [25] of E_i and $\mathcal{S}_i$, and assuming all the $l=5$ strength has been observed, one concludes that the $0h_{11/2}$ level is bound by 4.5 MeV.

From a comparison of the SOM and EXP columns in Fig. 12, it is clear that there is good agreement for the states with $l\leq 2$—in these cases the rms deviation between theory and experiment is 400 keV. An increase in the spin-orbit force would improve the situation for the $l=4$ and 5 states, provided the parameters of the Woods-Saxon well, shown in Fig. 11, were not appreciably changed. A stronger spin-orbit interaction, which would be consistent with the ^{89}Y results of Honoré *et al.* [39], would lead to tighter binding of the $0g_{9/2}$ and $0h_{11/2}$ states, would push up the $0g_{7/2}$ state, and would have a minimal effect on the low-spin levels with $l\leq 2$. However, because the $0f$ levels are tightly bound, they would be less affected by the surface-peaked Thomas term. Thus, the $0f_{7/2}$ level would still be too loosely bound, and certainly the $0f_{5/2}$ level would be pushed up. Consequently, a simple increase in the spin-orbit force alone will not be sufficient to bring theory and experiment into better agreement for all bound states.

B. DOM

In the analysis of neutron-scattering data using the DOM the usual Woods-Saxon real well has added to it a real surface term whose strength is given by Eq. (10). In the bound-state regime we again assume a real surface term whose strength is determined by Eq. (10), but in this case the geometry of the well is taken, somewhat arbitrarily, to have the values of a_W and r_W that arise when $E=0$. These terms should be added to the real Woods-Saxon well listed under DOM in Table III. However, as we shall subsequently discuss, much better agreement with the bound-state data is obtained when the slight E dependence of r_V is ignored. The results, shown in Fig. 12 under the column headed DOM, were obtained when the real Woods-Saxon potential for negative energies is given by $J_V=(457.7-3.41E)$ MeV fm^3 (the value appropriate to ^{90}Zr), the geometries have the $E=0$ DOM values given in Table III, and the spin-orbit interaction has the Thomas form with the parameters of Eq. (1). From Fig. 12 it is clear that going from the SOM to the DOM changes the s and d states insignificantly, provides a distinct improvement for both f and g levels, and only slightly deteriorates the prediction of the $h_{11/2}$ binding. On the other hand, the $1p_{1/2}$ and $1p_{3/2}$ binding energies are significantly worsened, the former now being overbound by 1.3 MeV and the latter by 2.1 MeV. Overall, the general description of particle and hole-state binding energies is slightly better using the DOM than the SOM—for the former the rms deviation between theory and experiment is 1.2 MeV, whereas for the latter it is 1.4 MeV.

To use the DOM consistently, one should have taken into account the small energy variation of r_V given in Table III. Since the particle states have small values of E, the effect on them of including this energy dependence is unimportant. On the other hand, the continued increase of r_V with increasing binding energy has a devastating effect on the hole-state predictions: the rms deviation between theory and experiment is increased from the constant r_V value of 1.2 to 3.2 MeV. As an alternative, one might assume that r_V has the same energy dependence as given in Table III, but is symmetric about the Fermi energy E_F. If this is done, the rms deviation of the hole states shrinks 2.1 MeV, but still remains much worse than the constant r_V value.

In evaluating the strength of the added surface potential we have assumed that, for $E>24$ MeV, W decreases linearly with increasing E, becoming zero at 60 MeV and at higher energies. In order to check the sensitivity of bound-state predictions to this somewhat arbitrary assumption, we have redone the calculation assuming that W becomes zero at 150 MeV. With this change, the particle states become more tightly bound and the hole states more loosely bound. However, the effect is small: the $0g_{7/2}$, $0h_{11/2}$, $1d_{3/2}$, $2s_{1/2}$, and $1d_{5/2}$ particle states change by 0.05, 0.12, 0.06, 0.05, and 0.04 MeV, respectively, whereas the $0g_{9/2}$, $1/p_{1/2}$, $1p_{3/2}$, $0f_{5/2}$, and $0f_{7/2}$ hole states shift by 0.02, 0.06, 0.07, 0.04, and 0.10 MeV, respectively.

More important for the bound-state problem is the behavior of J_S at low scattering energies. Unfortunately, because of fluctuations, it is difficult to pin this behavior down. Although it is not shown explicitly for the DOM, the behavior is quite similar to that obtained for the SOM, shown in Fig. 3. From these results, it would appear that between 1.65 and 3.1 MeV J_S increases with E, between 3.1 and 5 MeV it decreases, and then for $E > 5$ MeV it again increases with energy. Assuming these variations are not a manifestation of fluctuations, we have fitted J_S with the expression $J_S = \alpha + \beta E$ independently in the three different energy intervals 0–3.1, 3.1–5, and 5–24 MeV, and investigated the change brought about in the predicted binding energies. The effect is in the opposite direction to that discussed in the preceding paragraph: all of the particle states are less tightly bound, and with the exception of the $0f_{7/2}$ level, the hole states are more tightly bound. The magnitude of the effect is larger than that in the above paragraph: the $0g_{7/2}$, $0h_{11/2}$, $1d_{3/2}$, $2s_{1/2}$, and $1d_{5/2}$ particle and the $0f_{7/2}$ hole states are less tightly bound by 0.33, 0.35, 0.38, 0.35, 0.26, and 0.10 MeV, respectively, whereas the $0g_{9/2}$, $1p_{1/2}$, $1p_{3/2}$, and $0f_{5/2}$ hole states are more tightly bound by 0.14, 0.29, 0.25, and 0.19 MeV, respectively. Although the predicted binding energies of the $0g_{7/2}$, $1d_{3/2}$, and $2s_{1/2}$ states are now closer to experiment, those of the $0h_{11/2}$ and $1d_{5/2}$ states are worsened, so that the rms deviation between theory and experiment is essentially the same as for the original calculation. On the other hand, the increase in the binding of the hole states worsens the agreement between theory and experiment—the rms deviation is now 1.4 MeV compared to 1.2 MeV for the results shown in Fig. 12.

Thus, it is concluded that the extrapolation of the neutron-scattering potential to the bound-state regime meets with only modest success. The energy-independent version of the DOM provides a significantly better picture of the bound-state data than do the two r_V-energy-dependent versions discussed, and it is also slightly better at describing the experimental results than is the SOM model.

VII. SUMMARY DISCUSSION

When the spin-orbit interaction of Eq. (1) is combined with SOM or DOM parameters given in Table III, a good description of both the elemental zirconium differential elastic scattering and neutron total cross sections between $\lesssim 1$ and 24 MeV is obtained. From Table III, it is evident that the volume integral per nucleon of the DOM real potential is smaller in magnitude and less energy dependent than its SOM counterpart. This is consistent with the fact that the added surface component ΔJ_S has the same sign and energy slope as J_{eff}. Thus, although ΔJ_S is only about 5% of the total J_V, it appears that about 30% of the E dependence of J_V in the conventional SOM is due to the dispersion-integral contribution. As discussed in Ref. [32], it is also clear that use of the DOM should decrease the energy dependence of r_V relative to that of the SOM, and indeed, this is true. However, a small but significant E dependence of r_V remains when the DOM is used. Finally, for both models a_V is energy independent, and its SOM and DOM values differ by a small percentage that is probably not significant.

In a recent paper [48], the dependence of the SOM r_V and J_V on mass number was studied at 8 MeV. Over the range $A = 51$ to 209, it was found that both r_V and J_V decrease with increasing A. The 8-MeV values found in the present SOM interpretation fit nicely into the systematics of Ref. [48], and the present a_V is nearly identical to the average value, 0.67 fm, found for the $A = 51$ to 209 nuclei. Since the SOM real potential is the sum of a smooth Hartree-Fock term and a nucleus-dependent dispersion contribution, one might have expected some deviation from the smooth A dependence that was found. However, as already noted, the dispersion-integral contribution is only about 5% of J_V, and also, as can be seen from Fig. 9, at 8 MeV ΔJ_S, is almost zero.

Turning to the imaginary potential, one sees from Table III that for both the SOM and the DOM r_W decreases with increasing energy, whereas a_W increases. This behavior has been already noted in our analysis of the neutron-scattering data for other nuclei [42,48–52] (^{51}V, ^{58}Ni, ^{59}Co, ^{89}Y, ^{115}In, and ^{209}Bi). As expected, J_S increases with energy since at higher energies more inelastic channels are open. Up to and including the 24-MeV data, we find no evidence for volume absorption, and this is consistent with the findings of Wang and Rapaport [5] who studied 24-MeV scattering from separated zirconium isotopes. From our work on elemental zirconium, we can say nothing about the isotopic behavior of the potential. However, from the work of Wang and Rapaport [5], it is clear the J_S increases with increasing $(N-Z)/A$ [see Eq. (5)]. This result has been found for other nuclei near closed shells [9], and reflects the fact that there the number of open channels is at a minimum. This finding is contrary to the $(N-Z)/A$ dependence of J_S proposed in global models [6,7], and again points at the fact that the imaginary potential is nuclear-structure dependent.

When the $(N-Z)/A$ dependence of the potentials, given by Eqs. (4) and (5), is invoked, our model describes quite well the elastic scattering from the various Zr isotopes (see Figs. 5 and 6). At low energies, compound-nucleus inelastic scattering to individual levels is predicted to be fairly large and agrees reasonably well with the elemental and isotopic experimental data (see Figs. 2 and 7). At higher energies, experimental resolution limits our inelastic-scattering results to groups consisting of contributions from several isotopes. Inelastic scattering to both the 1.85–2.2- and 2.6–2.9-MeV groups is predicted to be $\gtrsim 100$ mb on the basis of compound-nucleus theory, and this is in reasonable agreement with experiment. On the other hand, the predicted compound-nucleus cross section for the excitation of the 941-keV "level" is much smaller than observed, clearly indicating a large direct-reaction component. Its required magnitude is about the same as that found by Wang and Rapaport [5] for scattering to the yrast 2^+ states in ^{92}Zr and ^{94} Zr.

The real optical-model potentials have been extrapolated to negative energies, and the predicted binding energies of single-particle and -hole states of ^{90}Zr are compared with experiment in Fig. 12. In the SOM, this potential was assumed to have a Woods-Saxon form with the parameters shown in Fig. 11. In this case, the rms deviation between theory and experiment is 1.4 MeV for the particle states, and the same magnitude was found for the hole states. For the DOM, the shell-model potential is a sum of two terms: a Woods-Saxon well whose parameters are given in the caption of Fig. 12, plus a derivative Woods-Saxon well whose strength is determined by the dispersion relationship, Eq. (8), and whose geometry is given in Table III at $E=0$. The DOM description of the binding energies is somewhat better than obtained with the SOM model—the rms deviation of both the particle and hole states is 1.2 MeV. Delaroche *et al.* [4] have also studied the bound-state problem using a DOM determined from a fit to their ^{90}Zr data. With their interaction the predicted particle states are somewhat closer to experiment—the rms deviation is 0.8 MeV. On the other hand, their predicted hole states have an rms deviation of 2 MeV.

In determining the binding energies of the ^{90}Zr states it was assumed that all the stripping and pickup strength had been observed. Any missed stripping strength would imply looser binding for the particle states, and any missed pickup strength would lead to tighter hole-state binding. With the exception of the $0h_{11/2}$ level, both our calculations and those of Delaroche *et al.* [4] predict particle states more tightly bound than experiment. Thus, except for the $0h_{11/2}$, any missed stripping strength would worsen the agreement between theory and experiment for the particle states. On the other hand, with the exception of the $0g_{9/2}$ state, all hole states are predicted to be too tightly bound on the basis of both our DOM and that of Delaroche *et al.* Thus, missed pickup strength would improve the agreement between theory and experiment for all the hole states except the $0g_{9/2}$. For the SOM, shown in Fig. 12, only the $1p_{3/2}$ state is predicted to be too tightly bound, so for this model missed pickup strength would worsen the agreement between theory and experiment. Thus it would appear that, even with the optimum scenario on missed stripping and pickup strengths, the extrapolation of the ^{90}Zr scattering potential to the bound-state regime leads to predictions for binding energies that are considerably worse than were obtained, for example, from a similar extrapolation [42] in ^{51}V. In this latter case, the rms deviation between theory and experiment for the particle states was 550 keV, and for the hole states 700 keV.

The data [39] on the neighboring nucleus ^{89}Y indicates that the spin-orbit strength may be slightly larger than given by Eq. (1), and indeed, two recent analyses [4,5] of zirconium data have used a larger value for this interaction. Although the values of the spin-orbit parameters [Eq. (1)] are within the uncertainties given in the ^{89}Y analysis, we have redone the DOM interpretation using the strength determined from studies of this neighboring nucleus [39]. As shown in Fig. 10, the low-energy neutron total cross sections predicted by this model are substantially smaller than experiment. This shortcoming is mainly due to the small value of r_V at low energies in this model: models based upon low-energy data, for example, that of Moldauer [53], generally lead to r_V values in the neighborhood of 1.3 fm. When the potentials described by Eqs. (14) and (15) are extrapolated to the bound region and $E=0$ values are used for $V_{\mathrm{s.o.}}$, r_V, r_W, and a_W, all states except the $1p_{3/2}$ are predicted to be less tightly bound than experiment because of the very slow increase in J_V with decreasing energy. This actually lowers the rms deviation between theory and experiment for the particle states to 0.8 MeV, but worsens the predictions for the hole states to an rms deviation of 1.7 MeV. Thus, if zirconium data are to be analyzed using the DOM the parameters of Table III and the spin-orbit strength of Eq. (1) should be used.

Finally, most of the parameters of the above SOM and DOM have energy dependences that are reasonably represented by linear expressions. These are clearly first approximations, valid only over the energy range of the present interpretations, and should not be used to extrapolate to far higher energies. It is reasonable to expect that energy-independent values are asymptotically approached above 20 to 25 MeV. This transition may already be underway between 10 and 24 MeV, but it is impossible to tell due to absence of experimental information in this energy region.

ACKNOWLEDGMENTS

This work was supported by the U.S. Department of Energy under Contract No. W-31-109-Eng-38.

---

[1] P. E. Hodgson, *Nuclear Reactions and Nuclear Structure* (Clarendon, Oxford, 1971).

[2] G. R. Satchler, *Direct Nuclear Reactions* (Clarendon, Oxford, 1983).

[3] A. M. Lane, Phys. Rev. Lett. **8**, 171 (1962).

[4] J. P. Delaroche, Y. Wang, and J. Rapaport, Phys. Rev. C **39**, 391 (1989).

[5] Y. Wang and J. Rapaport, Nucl. Phys. **A517**, 301 (1990).

[6] R. L. Walter and P. P. Guss, in *Proceedings of the Conference on Nuclear Data for Basic and Applied Science*, edited by P. Young, R. Brown, G. Auchampaugh, P. Lisowski, and L. Stewart (Gordon and Breach, New York, 1986), Vol. 2, p. 1079.

[7] J. Rapaport, Phys. Rep. **87**, 25 (1982).

[8] R. D. Lawson, P. T. Guenther, and A. B. Smith, Nucl. Phys. **A519**, 487 (1990).

[9] A. M. Lane, J. E. Lynn, E. Melkonian, and E. Rae, Phys. Rev. Lett. **2**, 424 (1959); W. Vonach, A. B. Smith, and P. A. Moldauer, Phys. Lett. **11**, 331 (1964).
[10] P. E. Hodgson, private communication.
[11] C. Mahaux and H. Ngo, Phys. Lett. **100B**, 285 (1981); Nucl. Phys. **A378**, 205 (1982).
[12] C. Mahaux and R. Sartor, Phys. Rev. Lett. **57**, 3015 (1986).
[13] C. Mahaux and R. Sartor, in *Advances in Nuclear Physics,* edited by J. W. Negele and Erich Vogt (Plenum, New York, in press).
[14] A. Smith, P. Guenther, R. Larson, C. Nelson, P. Walker, and J. Whalen, Nucl. Instrum. Methods **50**, 277 (1967).
[15] C. Budtz-Jorgensen, P. Guenther, A. Smith, J. Whalen, W. McMurray, M. Renan, and I. Van Heerden, Z. Phys. **A319**, 47 (1984).
[16] S. Chiba, P. T. Guenther, and A. B. Smith, Argonne National Laboratory Report ANL/NDM-112, 1990.
[17] M. Drosg, Production of Monoenergetic Neutrons Between 0.1 and 23 MeV: Neutron Energies and Cross Sections, IAEA-TECDOC-410, 239 (IAEA, Vienna, 1987).
[18] A. Smith, P. Guenther, and R. Sjoblum, Nucl. Instrum. Methods **140**, 397 (1977).
[19] *Nuclear Standard File,* IAEA Technical Report No. 227, edited by H. Conde, A. Smith, and A. Lorenz (IAEA, Vienna, 1983).
[20] A. B. Smith, P. T. Guenther, and R. D. McKnight, in *Proceedings of the Conference on Data for Science and Technology,* edited by K. H. Böckhoff (Reidel, Dordrecht, Holland, 1982), p. 39.
[21] P. T. Guenther, PhD. thesis, University of Illinois, 1977.
[22] A. B. Smith, Monte Carlo correction computer codes MONTE-SPHERE and MONTE-POLY, unpublished memoranda (1988) available from the author.
[23] A. B. Smith and P. T. Guenther, Argonne National Laboratory Report ANL/NDM-69, 1982.
[24] D. C. Kocher, Nucl. Data Sheets **16**, 55 (1975).
[25] H. W. Muller, Nucl. Data Sheets **31**, 181 (1980); **60**, 835 (1990).
[26] P. Luksch, Nucl. Data Sheets **30**, 573 (1980).
[27] H. W. Muller, Nucl. Data Sheets **44**, 277 (1985).
[28] *Chart of the Nuclides,* 13th ed., prepared by F. W. Walker, D. G. Miller, and F. Feiner (General Electric Co., 175 Curtner Ave. Mail Code 684, San Jose, CA, 95125, 1983).
[29] P. A. Moldauer, private communication (1982) as modified by S. Chiba (1989).
[30] W. Hauser and H. Feshbach, Phys. Rev. **87**, 366 (1952).
[31] P. A. Moldauer, Nucl. Phys. **A344**, 185 (1980).
[32] S. Chiba, P. T. Guenther, A. B. Smith, M. Sugimoto, and R. D. Lawson, Argonne National Laboratory Report ANL/NDM-119, 1991.
[33] S. Chiba, P. T. Guenther, J. W. Meadows, R. D. Lawson, A. B. Smith, D. L. Smith, and R. J. Howerton, Argonne National Laboratory report (to be published); A. B. Smith, P. T. Guenther, and J. F. Whalen, Argonne National Laboratory Report ANL/NDM-4, 1974.
[34] A. Gilbert and A. Cameron, Can. J. Phys. **43**, 1446 (1965).
[35] S. F. Mughabghab, M. Divadeenam, and N. E. Holden, *Neutron Cross Sections* (Academic, New York, 1981).
[36] S. Tanaka, Data available at the National Nuclear Data Center, Brookhaven National Laboratory.
[37] R. W. Stooksberry, J. H. Anderson, and M. Goldsmith, Phys. Rev. C **13**, 1061 (1976).
[38] F. D. McDaniel, J. D. Brandenberger, G. D. Glasgow, and H. G. Leighton, Phys. Rev. C **10**, 1087 (1974).
[39] G. M. Honoré, R. S. Pedroni, C. R. Howell, H. G. Pfutzner, R. C. Byrd, G. Tungate, and R. L. Walter, Phys. Rev. C **34**, 825 (1986).
[40] C. Mahaux and R. Sartor, Nucl. Phys. **A468**, 193 (1987).
[41] C. Mahaux and R. Sartor, Phys. Rev. C **36**, 1777 (1987).
[42] R. D. Lawson, P. T. Guenther, and A. B. Smith, Nucl. Phys. **A493**, 267 (1989).
[43] C. Mahaux and R. Sartor, Nucl. Phys. **A484**, 205 (1988).
[44] G. E. Brown and M. Rho, Nucl. Phys. **A372**, 397 (1981).
[45] A. Graue, L. H. Herland, K. J. Lervik, J. T. Nesse, and E. R. Cosman, Nucl. Phys. **A187**, 141 (1972).
[46] A. H. Wapstra and K. Bos, At. Data Nucl. Data Tables **19**, 177 (1977).
[47] J. Kasagi, G. M. Crawley, E. Kashy, J. Duffy, S. Gales, E. Gerlic, and D. Friesel, Phys. Rev. C **28**, 1065 (1983).
[48] S. Chiba, P. T. Guenther, R. D. Lawson, and A. B. Smith, Phys. Rev. C **42**, 2487 (1990).
[49] A. B. Smith *et al.* (in preparation).
[50] A. B. Smith, P. T. Guenther, and R. D. Lawson, Nucl. Phys. **A483**, 50 (1988).
[51] R. D. Lawson, P. T. Guenther, and A. B. Smith, Phys. Rev. C **34**, 1599 (1986).
[52] R. D. Lawson, P. T. Guenther, and A. B. Smith, Phys. Rev. C **36**, 1298 (1987).
[53] P. A. Moldauer, Nucl. Phys. **47**, 65 (1963).